Laser Power Efficiency of Partial Histogram Direct Time-of-Flight Lidar Sensors

Laser Power Efficiency of Partial Histogram Direct Time-of-Flight Lidar Sensors

Filip Taneski, Tarek Al Abbas, *Member, IEEE,* and Robert K. Henderson, *Fellow, IEEE*

***Abstract*—On-chip capacity for storing temporal photon data in direct time-of-flight (dToF) lidar sensors is limited. This has prompted the development of various partial histogram approaches to reduce the amount of data stored on-chip. The aim of this paper is to inform sensor design by providing a taxonomy of these approaches, models for evaluating their impact on system laser power and identification of additional trade-offs which must be considered. All published on-chip partial histogram lidar approaches to-date are reviewed and two main categories are established: *zooming* and *sliding*. A means of evaluating any specific configuration based on its histogram reduction ratio (HRR) is also established. To quantitatively evaluate partial histogram approaches, a model to determine the minimum number of required laser cycles is developed. Both zooming and sliding are compared to an ideal baseline using this model, in order to establish a laser power penalty benchmark for each approach. These are evaluated over a range of real-world design conditions for two contrasting designs: short-range indoor and long-range outdoor. In general, a sliding approach is found to be the most laser power-efficient for long-range outdoor applications, while a zooming approach becomes increasingly more effective under low ambient conditions. Power efficient *cycle-scaled* variations on the conventional zooming and sliding approaches are introduced. These are shown to consistently reduce the laser power penalty across all tested design conditions. It is also shown that a cycle-scaled sliding histogram approach can be adopted to reduce the required on-chip histogram storage capacity by half, with almost no additional laser power penalty. Finally, a qualitative discussion of zooming and sliding compares additional key design considerations such as sensitivity to motion artefacts.**

***Index Terms*—Direct time-of-flight (dToF), light detection and ranging (LiDAR), 3-D ranging, CMOS image sensor (CIS), distance measurement, single-photon avalanche diode (SPAD), time-of-flight (ToF).**

I. INTRODUCTION

DIRECT time-of-flight (dToF) lidar is a technique used to determine distance, by measuring the roundtrip time of a laser pulse. Commercial interests are motivated by applications such as 3D facial recognition [1], augmented and virtual reality (AR/VR) [2] and, more recently, advanced driver-assistance systems (ADAS) for self-driving vehicles [3].

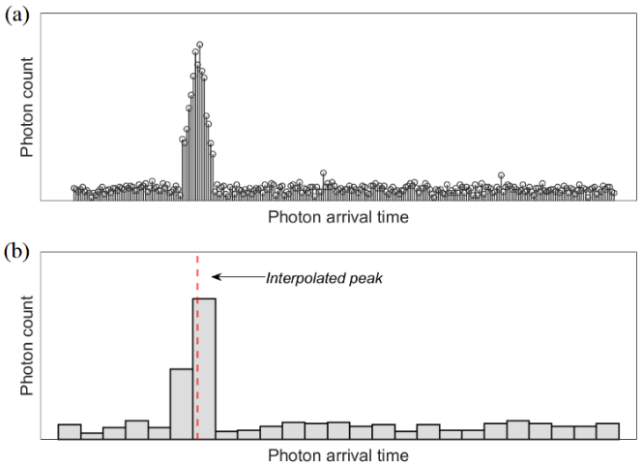

Fig. 1. Compression of raw photon arrival time data (a) into a histogram (b) and peak interpolation to recover precision.

The earliest implementations began with single-point laser rangefinders in 1960 by Hughes Aircraft Company [4] and the first laser distance measurement to Earth's moon by MIT in 1962 [5]. Through to the 1990s, technology scaling along with continued interest in space navigation, defense and robotics enabled development of compact 2D scannable point lidars [6].

By the end of the 1990s, the first flash lidar was developed at Advanced Scientific Concepts [7] using a 2D array of sensors pixels, each independently measuring the laser return time. This made 3D ranging possible without the need for mechanical scanning.

In 2003, the fabrication of single-photon avalanche diodes (SPADs) using standard CMOS processes was achieved [8], allowing commercially-feasible single-photon sensitivity alongside integrated CMOS circuitry. Before long, the integration of SPADs alongside photon arrival timing circuitry was realized [9]. This was shortly followed by the addition of memory to collect and store multiple time stamps over successive cycles [10]. The scaling of CMOS technologies and the adoption of 3D chip stacking, now enables large 2D arrays of SPAD sensors to be integrated onto a single silicon chip [11].

This paragraph of the first footnote will contain the date on which you submitted your paper for review, which is populated by IEEE. It is IEEE style to display support information, including sponsor and financial support acknowledgment, here and not in an acknowledgment section at the end of the article. For example, "This work was supported in part by the U.S. Department of Commerce under Grant BS123456." The name of the corresponding author appears after the financial information, e.g. *(Corresponding author: M. Smith).* Here you may also indicate if authors contributed equally or if there are co-first authors.

Filip Taneski and Robert K. Henderson are with the University of Edinburgh, Edinburgh, EH9 3JL, U.K. (e-mail: filip.taneski@ed.ac.uk; robert.henderson@ed.ac.uk).

Tarek Al Abbas is with Ouster Automotive, Edinburgh, U.K. (e-mail: tarek.alabbas@ouster.io).

Color versions of one or more of the figures in this article are available online at http://ieeexplore.ieee.org

However, as the number of pixels on a flash lidar sensor increases, storing and processing all photon events off-chip becomes less feasible. Instead, storing and/or processing of this data, for every pixel, must be done on the sensor itself. An effective method to compress photons data is to sort photon arrival times into coarse histogram bins, as illustrated in Fig. 1. Precision can then be recovered through interpolation. This approach was adopted in a 64×64 dToF pixel sensor using 16 bins per pixel to range up to 50m [12] and in a 16-pixel dToF sensor using 2048 bins per pixel to range up to 100m [13]. Nevertheless, the data capacity of each pixel is limited, leading to a trade-off between distance resolution (histogram bin width) and the maximum measurable distance (total histogram bins).

To overcome this constraint, a series of novel *partial histogram* approaches have recently been developed. These approaches, described in detail in Section II, successfully reduce the amount of data stored and processed on-chip per frame. However, the consequence of each approach, is a substantial increase in the number of laser cycles required for the lidar system to detect a target.

The average optical power of a pulsed laser P_{avg} with rectangular pulse width τ, laser cycle rate f_{cycle} and peak optical power P_{peak} is given by

$$P_{avg} = \tau f_{cycle} P_{peak} \quad (1)$$

If the use of a partial histogram approaches results in a lidar system which requires additional laser cycles, the sensor activity and minimum achievable frame rate will be severely impacted. Above all, the resulting increase in average laser power would have severe repercussions. This is particularly crucial in flash lidar where the laser can contribute as much as 80% of the total system power consumption [14]. Therefore, any design decisions taken to reduce on-chip capacity must consider the resulting impact of increased laser power, which to-date has not been studied.

This paper contributes to the state-of-the-art by enabling informed design of partial histogram dToF sensors based on laser power impact. A model is presented to allow the laser power-efficiency of partial histogram approaches to be evaluated and *cycle-scaled* variants are proposed to significantly reduce laser power. The paper is organized as follows:

- Section II: a taxonomy and literature review of on-chip partial histogram implementations to-date.
- Section III: a model for determining the minimum number of laser cycles required for any dToF system.
- Section IV: analysis of partial histogram approaches based on the minimum number of laser cycles required to achieve real-world design specifications. The benefits of cycle-scaled approaches are also evaluated.
- Section V: a power penalty comparison of partial histogram approaches and a discussion of additional key considerations to inform design decisions.

II. A Review of Partial Histogram Lidar Sensors

The aim of partial histogram approaches is to reduce the total number of histogram bins that would otherwise be needed to achieve a given range or precision. The term *histogram reduction ratio* (HRR) is introduced to describe the ratio of bin reduction that is achieved for a given approach.

All partial histogram approaches adopted to-date can be categorized into two groups: *zooming* and *sliding*. These are illustrated in Fig. 2.

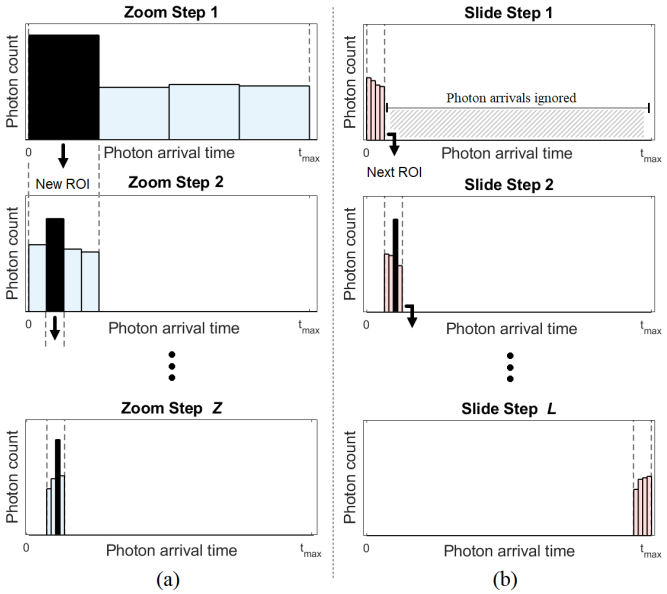

Fig. 2. Illustration of partial histogram methods (a) *zooming* over "Z" steps and (b) *sliding* over "L" steps.

A. Zooming Histogram

In a zooming approach, the lidar sensor begins by spreading the reduced set of histogram bins across the full distance range. After an initial series of laser cycles, the peak bin is identified, establishing a region-of-interest (ROI). In the next step, the histogram sensing range is zoomed in to count photons within only the identified ROI, improving the distance resolution. Multiple zooming steps Z can be employed until the desired resolution is achieved, as illustrated in Fig. 2(a). A zooming histogram architecture using M bins at each step achieves a histogram reduction ratio of:

$$\text{HRR} = M/M^Z \quad (2)$$

The first histogram-per-pixel SPAD sensor capable of zooming both time resolution and position was published in [15] where 32 histogram bins can be programmed to a width of between 50 ps and 6.4 ns. This early implementation requires the time resolution and position of histogram bins to be programmed externally between each zoom step. In addition, histogram settings can only be applied globally across all pixels. This makes it practical for the targeted application of spectroscopy but is less suited to applications such as lidar.

The first sensor in which each pixel is able to independently zoom to a specific region-of-interest was published in [16]. In this implementation each pixel uses 8 histogram bins over 3

zooming steps to achieve a HRR of 1/64. A maximum range of 50 m with 8.8 cm accuracy and worst-case precision of 1.4 mm (single standard deviation) is achieved, although the frame rate in this configuration was not disclosed. This implementation is further developed in [17] where 2 stages of 32 bins are used, giving a HRR of 1/32. A maximum range of 9.5 m with an accuracy of 1 cm and precision of 9 mm is achieved. Similarly, the frame rate under this specific performance is not disclosed, although an achievable frame rate of 20 fps is reported.

In [18], each pixel uses only 2 histogram bins but over a total of 8 zooming steps per frame to achieve a HRR of 1/128, effectively trading off on-chip storage capacity for frame rate. A maximum sensing distance of 45 m is achieved with 4 cm accuracy and a precision of 40 cm. Adoption of a large number of zooming steps in this implementation is likely to severely limit frame rate, which is not disclosed. To improve frame rate, the design is further developed in [19], increasing the number of bins in each step from 2 to 4 and reducing the number of zooming steps from 8 to 4. To mitigate the effect of edge-cases, the final (fine) zoom step covers half the range of the previous course step rather than a quarter. As a result, this design also achieves a HRR of 1/32.

Finally, a two-step zooming approach is implemented in [20] where each pixel begins with a coarse 5-bit step, followed by a fine 6-bit (64 bins) step, giving a HRR of 1/32 limited by the first coarse stage. Implemented as a scanning lidar sensor, it uses fewer pixels than an equivalent flash sensor, allowing for a larger number of bins to be integrated on-chip compared to the previously described sensors. A maximum range of 48 m is achieved at a frame rate of 1 fps with an accuracy of 11.86 cm and a precision of 0.85 cm. A summary of all published on-chip histogram zooming implementations is provided in Table I.

B. Sliding Histogram

In a sliding approach, the lidar sensor starts by spreading the reduced histogram across only a subset of the full sensing range. Thus, only a fraction of the full range is initially captured, albeit to a high level of precision. After sufficient cycles have been integrated, the ROI slides to a new range. This process is repeated until the full the distance range has been covered. Ignoring use of any overlap bins, a slide histogramming architecture achieves a histogram reduction ratio equivalent to the number of steps L.

The first implementation of a sensor with per-pixel sliding histograms was published in [14] where 32 histogram bins are used to slide across 16 time windows. 6 overlap bins are allocated on each side of the histogram to cover edge-cases, resulting in an equivalent of 320 time bins across the full sensing range, giving a HRR of 1/10. The system, targeted for indoor use, achieves 6 m range with 1% (6 cm) accuracy and a precision of 0.15% (9 mm) at a frame rate of 30 fps.

The sensor described in [21] uses 8 bins which can be configured as a sliding histogram with up to 128 steps i.e. minimum HRR of 1/128. However, since operating in a continuous sliding histogram mode is not the primary mode of acquisition for this sensor, performance under this configuration is not disclosed. The sensor in [22] is also capable of a sliding approach, referred to as progressive gating, whereby each sliding region-of interest is set globally across all pixels. Details of the number of achievable steps or sensor performance in this mode of operation are not disclosed.

A summary of histogram reduction configurations used in published sliding lidar sensors is provided in Table I. Sensors published in [23] and [24] are also notable early sliding implementations, though using a single time gate. These are omitted from the table which focuses on on-chip histogram implementations only.

TABLE I:
SUMMARY OF ON-CHIP PARTIAL HISTOGRAM CONFIGURATIONS USED IN LIDAR SENSOR PUBLICATIONS

Publication	[16]	[17]	[18]	[19]	[20]	[14]	[21]
Partial Histogram Method	Zooming					Sliding	
Bins	8	32	2	4	64	32	8
Steps	3	2	8	4	2	16	128
Histogram Reduction Ratio	$1/64$	$1/32$	$1/128$	$1/32$	$1/32$	$1/10$	$1/128$

C. Discussion

Both sliding and zooming successfully reduce histogram data, allowing extended dToF range and/or precision in spite of limited on-chip storage. However, both approaches incur a laser cycle penalty compared to counting all photon arrivals over the full distance range. In the case of zooming, this penalty arises from the wider time resolution of each bin in earlier zooming steps, which increases the number of background photons captured in each bin. Therefore, more laser cycles are required to identify each region-of-interest. In the case of sliding, returning signal photons are ignored in the majority of sliding steps, so a greater number of cycles are required to complete a full frame. Thus, compensating for limited on-chip photon storage by adopting partial histogram approaches impacts lidar system performance as a whole.

In the following section, a method for calculating the minimum number of laser cycles required to detect a target is presented. This will enable the performance of different partial histogram approaches to be evaluated in subsequent sections.

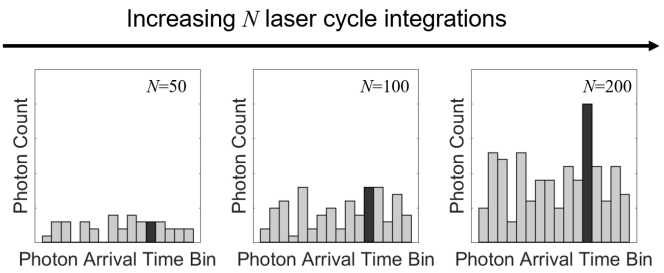

Fig. 3. The signal return time bin (black) becomes more distinguishable as the number of laser cycles increases.

III. Probability of Detection Model

For every pulse of the laser, a dToF sensor is exposed to both background and signal photons. In order to identify the signal, photons are accumulated over multiple N laser cycles per frame. In a high noise environment, such as outdoor dToF, determining the laser arrival time by identifying the peak histogram bin is a highly suitable approach [25]. However, as Fig. 3 illustrates, the peak histogram bin may not correspond to the signal bin if the number of integration cycles is insufficient. The proportion of frames in which the signal bin is correctly identified is known as the probability of detection P_D and depends on: (i) the expected signal photon count per laser pulse; (ii) the ambient background photon arrival rate; (iii) the number of laser integration cycles. This model aims to determine the limit of the minimum number of laser cycles required to meet a given probability of detection. Accordingly, the following assumptions are made:

- the laser signal falls entirely within a single time bin
- no SPAD dead time or pile-up
- all photon arrivals per cycle are counted

One method of characterizing probability of detection for a histogram-based dToF system is to run a time-intensive Monte Carlo simulation. In this approach, a Poisson-distributed background photon count is generated over M histogram bins. A Poisson-distributed signal photon count is then added to a single pre-determined bin. By observing the ratio of runs in which the signal bin contains the most photon counts, the probability of detection can be characterized.

To provide a more complete analysis over a time-intensive Monte Carlo approach, a derivation of probability of detection for histogram-based dToF is provided. Let λ_B represent the average background photon arrivals per bin after N cycles and λ_S the average signal photon arrivals after N cycles. For a system with M bins, P_D can be described as: the probability that the signal bin takes on a photon count value x *and* all $M-1$ non-signal bin take on a value lower than x, for all possible photon count values x:

$$P_D = \int f_S(x) \times F_B(x)^{M-1}\, dx \tag{3}$$

Here, $f_S(x)$ is the probability density function (PDF) of the signal bin and $F_B(x)$ is the cumulative density (CDF) of any non-signal bin. When approximated to a Gaussian distribution, these can be expressed as:

$$f_S(x) \approx \frac{1}{(\lambda_S+\lambda_B)\sqrt{2\pi}} e^{-\frac{1}{2}\left(\frac{x-(\lambda_S+\lambda_B)}{(\lambda_S+\lambda_B)}\right)} \tag{4}$$

$$F_B(x) \approx \Phi\left(\frac{x-\lambda_B}{\lambda_B}\right) \tag{5}$$

Recognizing that the photon count value x cannot take on negative values binds the lower limit of the integral in (3). The upper limit can be set by recognizing that values of x multiple times greater than $\lambda_S+\lambda_B$ result in negligible accuracy improvement.

This derivation is validated in Fig. 4 which shows the calculated probability of detection using (3) overlaid with the results generated through a Monte Carlo approach for a fixed λ_S and λ_B. Note that for low numbers of laser cycles N, the accuracy of (3) begins to diminish with respect to the Monte Carlo result as the assumption of Gaussian-distributed photon arrival rates becomes less valid. However, this is irrelevant in the context of dToF, where typically thousands of laser cycles are integrated per frame.

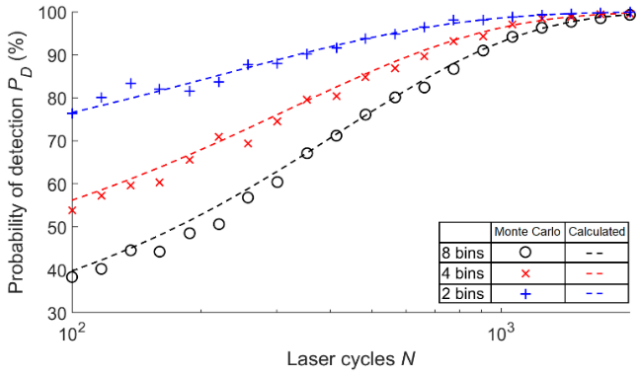

Fig. 4. Calculated probability of detection using (3) accurately reproduces the values of a Monte Carlo approach.

By applying standard computational optimization methods on (3), the minimum number of laser cycles N_{min} to detect a target for a given probability of detection; signal photon count; and background photon rate, can be determined. This provides a useful tool in the design of lidar systems and forms the basis for evaluating partial histogram approaches which follows.

IV. Analysis of Partial Histogram Approaches

A methodology for evaluating any histogram-based dToF design based on the minimum required number of laser cycles is outlined in **Fig. 5**. It is composed of the following:

1) **Lidar Design Specification**
   A set of system design parameters which determine the expected signal and background photon count.
2) **Photon Budget Model**
   Calculation of expected signal and background photon rates using the dToF numerical model developed in [26].
3) **Probability of Detection Model**
   Solves (3) using computational optimization methods to determine the minimum number of required laser cycles.

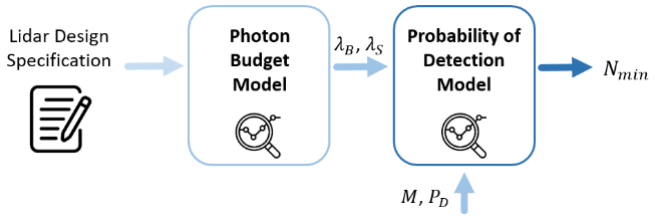

Fig. 5. Methodology for evaluating any histogram-based dToF design based on the minimum required number of laser cycles.

It should be highlighted that this model only provides the minimum number of laser cycles required for a lidar system to identify the correct temporal signal bin. To achieve a high degree of distance precision through interpolation, further laser cycles are often required, a topic thoroughly explored in [27]. The approach adopted here enables a universal comparison of partial histogram approaches without additional constraints.

TABLE II:
TWO CONTRASTING LIDAR DESIGN SPECIFICATIONS USED FOR ANALYSIS OF PARTIAL HISTOGRAM APPROACHES

Component	Parameter	Value	
		Short-range (SR) indoor	**Long-range (LR) outdoor**
Target	Maximum distance	10 m	200 m
	Reflectivity	10 - 90%	
Ambience	Intensity	2.5 - 25 klux	10 - 100 klux
	Irradiance reference	ASTMG173	
System	Probability of detection	99%	
	Frame rate	30 fps	
Emitter	Pulse energy	500 nJ	50 µJ
	Wavelength	905 nm	
	Spot shape	Round	
Sensor (achievable SPAD characteristics based on **[28]**)	Photon detection efficiency	22%	
	Pixel pitch	30 µm	
	SPADs per pixel	3 × 3	
	Pixel resolution	4×(200 × 63)	200 × 63
	Field-of-view	85° × 32°	26° × 8°
Lens	Diameter	6 mm	
	F#	1.1	2.2
	Filter bandwidth	20 nm	
	Transmission	1	

TABLE III:
EXPECTED PHOTON RATE FOR BOTH SR AND LR DESIGN SPECIFICATIONS AS GIVEN BY THE PHOTON BUDGET MODEL

		Reflectivity (%)	
		Min	**Max**
Ambient Intensity (klux)	**Min**	$\lambda_S = 0.01$ count $\omega_B = 2$M count/s	$\lambda_S = 0.09$ count $\omega_B = 18$M count/s
	Max	$\lambda_S = 0.01$ count $\omega_B = 20$M count/s	$\lambda_S = 0.09$ count $\omega_B = 180$M count/s

To evaluate and compare partial histogram approaches, two contrasting lidar design specification are modelled. These are outlined in Table II. The short-range (SR) set is typical of indoor applications such as AR/VR, while the long-range (LR) set resembles common requirements for fully autonomous self-driving vehicles. For a comprehensive evaluation of partial histogram approaches, the two designs are explored across the full range of min/max target reflectivity and ambient intensity.

The resulting average signal photon (λ_S) and background rate (ω_B) given by the photon budget model across this design space is summarized in Table III. Although two contrasting designs are presented, both exhibit equivalent signal and background photon return rates at the boundaries. For example, the LR design exhibits the same background return rate at 100 klux as the SR design at 25 klux due to a 2× increase in lens F#.

In the analysis which follows, each histogram approach will be evaluated based on the minimum number of laser cycles required to detect a target at the maximum distance with 99% probability of detection ($P_D = 0.99$).

The first phase of analysis begins by establishing a baseline level of performance for an ideal pixel with no capacity constraints. A capacity of M=1024 bins is assigned to cover the full distance range in this case. The resulting average background photon rate in each bin (λ_B) when all M bins are used to cover the maximum distance range (D_{max}) is given by (6) where c is the speed of light.

$$\lambda_B = \omega_B \frac{2\,D_{max}}{M\,c} \tag{6}$$

Solving the probability of detection model (3) for λ_B and λ_S across the full design space (Table III) to find the minimum required laser cycles gives the results shown in Fig. 6. The maximum laser cycle limit below-which the frame rate specification can be achieved is annotated and supported by both SR (500k cycles) and LR (25k cycles) designs across the full design space (assuming no frame time lost for readout).

Using the same method, the minimum number of laser cycles for equivalent partial histogram approaches are now analyzed.

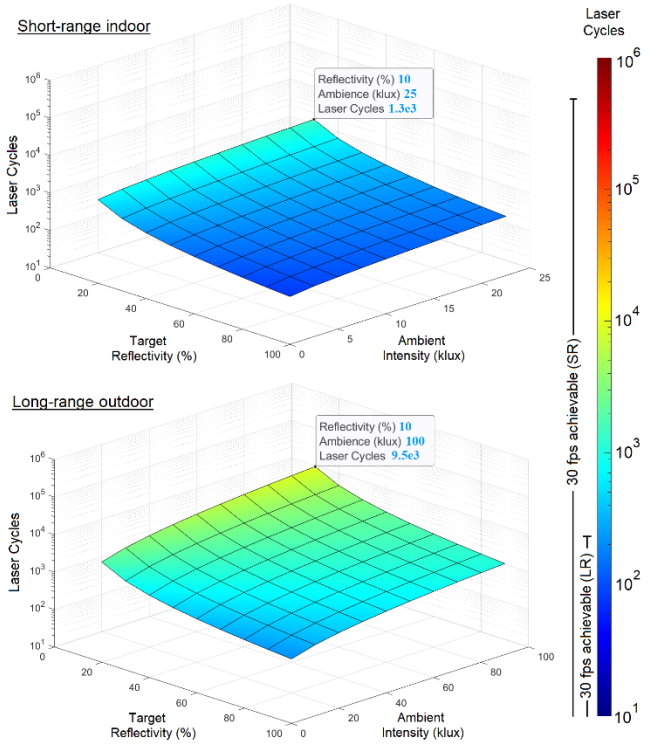

Fig. 6. Minimum number of laser cycles required for the ideal baseline pixel to meet the design specification in Table II.

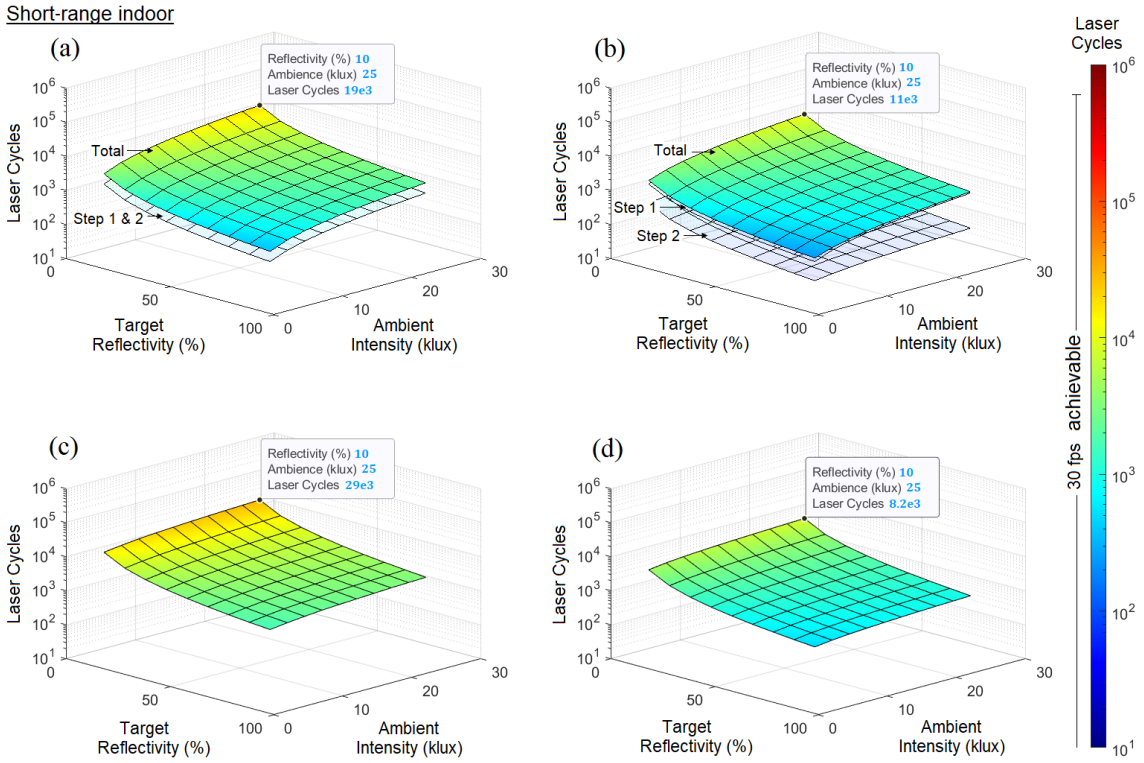

Fig. 7. The minimum number of laser cycles required for the short-range (SR) design in Table II to meet a set of target reflectivity and ambient intensity specifications using: (a) zooming (b) cycle-scaled zooming (c) sliding (d) cycle-scaled sliding.

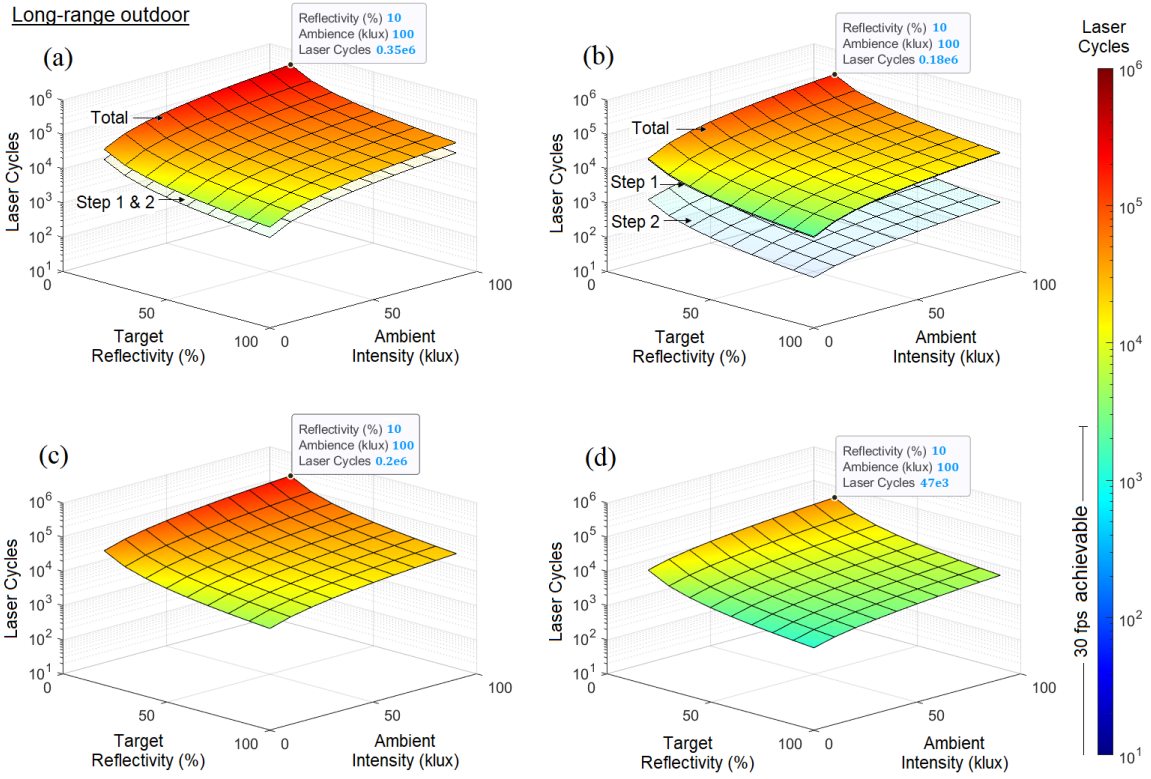

Fig. 8 The minimum number of laser cycles required for the long-range (LR) design in Table II to meet a set of target reflectivity and ambient intensity specifications using: (a) zooming (b) cycle-scaled zooming (c) sliding (d) cycle-scaled sliding.

A. Zooming Histogram Performance

To model zooming, pixel capacity is restricted to a more practical value of $M = 32$ bins. A total of 2 zoom steps (HRR = 1/32) results in a bin resolution during the final zoom step equivalent to the ideal baseline ($D_{max}/1024$). Assuming the number of laser cycles used at each zoom step is the same as the minimum required for the first zoom step, the background count per bin at each step is given once again by (6). The full design space of target reflectivity and ambient intensity is explored for the zooming pixel and the resulting minimum number of laser cycles is shown in Fig. 7(a) and Fig. 8(a) for the SR and LR designs, respectively. Results are presented for each zoom step separately and cumulatively. The increased bin width, and hence background arrival rate per bin, results in an almost 15× laser power increase for the SR design and 37× for the LR design, compared to the ideal pixel at the minimum target reflectivity and maximum ambient intensity design point. Furthermore, no data point along the design space allows the LR system to meet the frame rate specification.

B. Cycle-Scaled Zooming Histogram Performance

A key feature of zooming is that the bin width is progressively scaled down after each step. The background photon count per bin at each individual i step can therefore be more accurately realized as:

$$\lambda_{B,zoom}(i) = \omega_B \frac{2\,D_{max}}{M^i\,c} \tag{7}$$

As a result, a more laser-power efficient *cycle-scaled* zooming approach is explored, whereby the required minimum number of laser cycles at each step is scaled accordingly based on the reduced λ_B. The resulting minimum number of laser cycles for the SR and LR designs using a cycle-scaled zooming approach are presented in Fig. 7(b) and Fig. 8(b) and shown to reduce laser power by almost 2×. A small portion of the LR design space now also falls within the range required to meet the frame rate specification.

C. Sliding Histogram Performance

To enable a like-for-like comparison with zooming, the sliding histogram model is also restricted to $M = 32$ bins. A total of 32 sliding steps results in the same HRR of 1/32 and a bin resolution equivalent to both the zooming and ideal baseline configurations (assuming no overlap bins). Since the observation time window at each step is reduced by the total steps (L), the background photon count per bins is given by:

$$\lambda_{B,slide} = \omega_B \frac{2\,D_{max}}{L\,M\,c} \tag{8}$$

To determine the minimum total laser cycles, the minimum cycles required to detect an object in the furthest distance bin of the final (32nd) slide step is first calculated. This is then multiplied by the total number of steps (L). The results are presented in Fig. 7(c) and Fig. 8(c) for the SR and LR designs, respectively. A laser cycle increase of over 20× is observed for both designs compared to the ideal pixel at the minimum target reflectivity and maximum ambient intensity design point.

D. Cycle-Scaled Sliding Histogram Performance

The returning laser signal power in a lidar system follows the inverse square law. Therefore, assigning the same number of laser cycles to all slide steps is not the most laser power-efficient method. As with the zooming approach, a cycle-scaled approach is therefore again proposed; scaling down the number of cycles used at each step based on the expected signal count at the maximum distance of each step.

Given the expected signal rate $\lambda_S(L)$ in the last slide step L, the average signal rate in each i step can be scaled as follows:

$$\lambda_{S,slide}(i) = \lambda_S(L) \times \left(\frac{i}{L}\right)^2 \tag{9}$$

By appropriately scaling λ_S for each slide step based on (9), the resulting minimum number of laser cycles from a cycle-scaled sliding approach is presented in Fig. 7(d) and Fig. 8(d). A reduction in laser cycles of 4× is observed. Furthermore, a large portion of the design space now lies within the range required to meet the frame rate specification.

V. Power Penalty & Design Considerations

A. Laser Power Penalty vs. Design Condition

To determine the relative power penalty of each partial histogram approach, the minimum number of cycles required by both SR and LR designs across the entire design space (Fig. 7 and Fig. 8) is compared to the ideal baseline (Fig. 6). These results are summarized in Fig. 9. The independence of laser power penalty to target reflectivity allows the results to be summarized as a function of ambient intensity only.

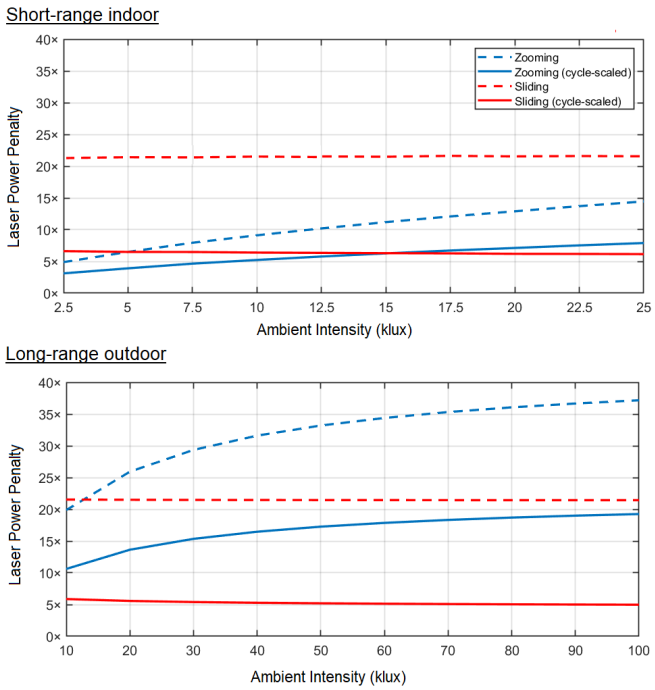

Fig. 9. Modelled laser power penalty of partial histogram approaches with an equivalent HRR of 1/32 for the designs outlined in Table II.

The relative power penalty of a sliding approach resolves to become largely independent of ambient intensity. This is due to the bin width in each step being the same as that in the equivalent ideal approach. Note the advantage of cycle-scaling in a sliding approach becomes slightly less significant under low ambient conditions where the minimum required number of laser cycles in close-range steps is already low.

On the other hand, zooming uses coarser bins compared to an equivalent ideal approach in all but the final zoom step. This makes identification of the signal bin in a zooming approach more sensitive to ambient levels relative to the ideal approach. As a result, the power penalty of zoom histogramming exhibits a strong dependence on the targeted ambient conditions.

For long-range outdoor lidar applications, Fig. 9 shows a cycle-scaled sliding approach to be the most laser power-efficient, regardless of ambient intensity conditions. For short-range indoor applications on the other hand, the use of a cycle-scaled zooming approach becomes more compelling, particularly under low ambient conditions where the region of interest at each step can be identified sooner.

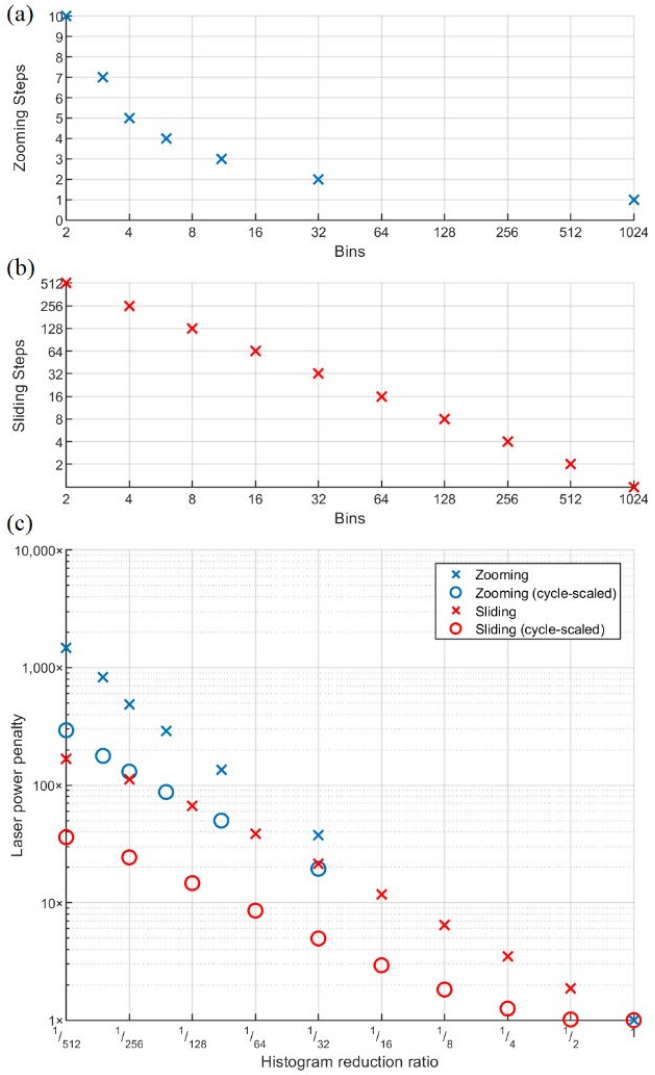

Fig. 10. (a) Zooming and (b) sliding configurations with equivalent effective bin width. (c) The resulting laser power penalty of each configuration as a function of HRR.

B. Laser Power Penalty vs. Histogram Reduction Ratio

To complete the quantitative analysis, the effect of different histogram reduction ratios is explored. This enables informed decisions based on specific on-chip capacity constraints for a given design. As before, the design conditions laid out in Table II are used. The design type (long-range), ambient intensity (100klux) and reflectivity (10%) remain fixed this time to simplify comparison. To maintain a consistent effective bin width, the bin/step combinations for each HRR have been carefully chosen and are outlined in Fig. 10(a) and (b) for zooming and sliding, respectively. The resulting power penalty as a function of HRR is shown in Fig. 10 (c). The plot shows that a sliding approach becomes increasingly more power-efficient over zooming for increasing HRR. This is a consequence of the ever-increasing bin width (and hence background count) of the first zoom step with additional steps.

A significant result observed in Fig. 10(c) is that the power penalty introduced through a cycle-scaled sliding approach with a HRR of ½ is almost negligible. By splitting the full histogram range into two steps, fewer competing bins are present in the second step, while cycle-scaling reduces the required number of cycles in the first step. This is an important observation, as it shows that dToF sensors can employ a cycle-scaled sliding approach to halve the required on-chip storage capacity while inflicting a negligible laser power penalty.

C. Other Design Considerations

Although this paper focuses on the laser power penalty introduced through both zooming and sliding, both approaches present further trade-offs which are now discussed.

Both partial histogram approaches can significantly reduce the number of histogram bins, and hence on-chip area, required to store photon data. However, a zooming approach would need to store higher count values compared to an equivalent zooming approach to accommodate a higher background photon count per bin in the first zoom step. On the other hand, a zooming approach only needs to readout histogram data after the final zoom step, whilst a sensor adopting a sliding approach needs to read out data after each consecutive step. For flash lidar sensors containing large pixel array, this may limit the achievable HRR using a sliding configuration.

A sliding approach needs to consider the event of an object moving between slide steps during acquisition, resulting in motion artefacts. Mitigating these effects requires the adoption of overlapping histogram regions and/or additional signal processing. The inherent nature of zooming to home in on a target can make it more robust against such artefacts.

The most contested drawback of zooming is its limitation in dealing with multi-peak events which can arise from multi-path reflections, multiple targets, or translucent objects in the line-of-sight such as glass. Although workarounds can be conceived to deal with such situations, these would inevitably require further on-chip storage resources and/or laser cycles.

Difficulties also arise in zooming when the returning laser arrival time lies between bins, causing a pixel to zoom in on the wrong region-of-interest. A sliding histogram approach can mitigate against such situations by allocated a small number of bins to an overlap region between steps. Designing an

equivalent solution for zooming is less trivial, particularly during earlier zoom steps.

A stoplight summary of both quantitative and qualitative evaluations is shown in Table IV.

TABLE IV
A STOPLIGHT SUMMARY OF DESIGN TRADE-OFFS FOR ZOOMING AND SLIDING HISTOGRAM APPROACHES

Parameter	Zooming	Sliding
Laser power penalty (low signal vs. background)	High	Low
Laser power penalty (high signal vs. background)	Low	Medium
Data rate	Low	High
Sensitivity to motion artefacts	Low	Medium
Sensitivity to inter-bin arrivals	Medium	Low
Sensitivity to multiple peaks	High	Low

VI. Conclusion

This paper presents an in-depth study of partial histogram lidar sensor approaches with a focus on laser power impact.

The first taxonomy of partial histogram has been conducted, establishing two categories: *zooming* and *sliding*. A means of evaluating any specific configuration based on its histogram reduction ratio (HRR) is also established and a literature review of all published partial histogram lidar sensors to-date is presented and summarized in Table I.

A relationship between probability of detection; average signal; background return; and the number of laser cycles in dToF lidar is derived (3). This enables evaluation of any histogram-based dToF design based on the minimum required number of laser cycles.

Power efficient cycle-scaled approaches of both zooming and sliding are proposed and shown to consistently reduce the laser power penalty across all tested design conditions. In general, a cycle-scaled sliding histogram approach exhibits the lowest power penalty in long-range outdoor applications while a zooming approach may be suitable for indoor-short range applications. A design sweet spot is identified, indicating that a cycle-scaled sliding approach with a HRR of ½ can allow the realization of a dToF sensor with half the required on-chip storage capacity, while inflicting a negligible laser power penalty. Additional key aspects to be considered when choosing between zooming and sliding approaches are discussed and summarized in Table IV.

VII. Acknowledgement

The authors would like to thank Ouster Automotive for funding this research, Salvatore Caporale and Joseph Briggs for contributing expertise in signal processing and statistics.

VIII. References

[1] S. Meers and K. Ward, "Face Recognition Using a Time-of-Flight Camera," in *2009 Sixth International Conference on Computer Graphics, Imaging and Visualization*, 11-14 Aug. 2009 2009, pp. 377-382, doi: 10.1109/CGIV.2009.44.

[2] I. Kim *et al.*, "Nanophotonics for light detection and ranging technology," *Nature Nanotechnology,* vol. 16, no. 5, pp. 508-524, 2021/05/01 2021, doi: 10.1038/s41565-021-00895-3.

[3] R. Roriz, J. Cabral, and T. Gomes, "Automotive LiDAR Technology: A Survey," *IEEE Transactions on Intelligent Transportation Systems,* vol. PP, 06/15 2021, doi: 10.1109/TITS.2021.3086804.

[4] G. Smith, "The early laser years at Hughes Aircraft Company," *IEEE Journal of Quantum Electronics,* vol. 20, no. 6, pp. 577-584, 1984, doi: 10.1109/JQE.1984.1072445.

[5] L. D. Smullin and G. Fiocco, "Optical Echoes from the Moon," *Nature,* vol. 194, no. 4835, pp. 1267-1267, 1962/06/01 1962, doi: 10.1038/1941267a0.

[6] A. Spring, "A History of Laser Scanning, Part 1: Space and Defense Applications," *Photogrammetric Engineering and Remote Sensing,* vol. 86, pp. 419-429, 08/14 2020, doi: 10.14358/PERS.86.7.1.

[7] R. Stettner, H. Bailey, and R. Richmond, *Eye-safe laser radar 3D imaging* (Aerospace/Defense Sensing, Simulation, and Controls). SPIE, 2001.

[8] A. Rochas *et al.*, "First fully integrated 2-D array of single-photon detectors in standard CMOS technology," *IEEE Photonics Technology Letters,* vol. 15, no. 7, pp. 963-965, 2003, doi: 10.1109/LPT.2003.813387.

[9] C. Veerappan *et al.*, "A 160×128 single-photon image sensor with on-pixel 55ps 10b time-to-digital converter," in *2011 IEEE International Solid-State Circuits Conference*, 20-24 Feb. 2011 2011, pp. 312-314, doi: 10.1109/ISSCC.2011.5746333.

[10] C. Niclass, M. Soga, H. Matsubara, M. Ogawa, and M. Kagami, "A 0.18µm CMOS SoC for a 100m-range 10fps 200×96-pixel time-of-flight depth sensor," in *2013 IEEE International Solid-State Circuits Conference Digest of Technical Papers*, 17-21 Feb. 2013 2013, pp. 488-489, doi: 10.1109/ISSCC.2013.6487827.

[11] T. Al Abbas, N. Dutton, O. Almer, S. Pellegrini, Y. Henrion, and R. Henderson, "Backside illuminated SPAD image sensor with 7.83µm pitch in 3D-stacked CMOS technology," 2016/12/3 2016, doi: 10.1109/IEDM.2016.7838372.

[12] S. W. Hutchings *et al.*, "A Reconfigurable 3-D-Stacked SPAD Imager With In-Pixel Histogramming for Flash LIDAR or High-Speed Time-of-Flight Imaging," *IEEE Journal of Solid-State Circuits,* vol. 54, no. 11, pp. 2947-2956, 2019, doi: 10.1109/JSSC.2019.2939083.

[13] C. Niclass, M. Soga, H. Matsubara, M. Ogawa, and M. Kagami, "A 0.18um CMOS SoC for a 100-m-Range 10-Frame/s 200x96-Pixel Time-of-Flight Depth

Sensor," *IEEE Journal of Solid-State Circuits,* vol. 49, no. 1, pp. 315-330, 2014, doi: 10.1109/JSSC.2013.2284352.

[14] D. Stoppa *et al.*, "A Reconfigurable QVGA/Q3VGA Direct Time-of-Flight 3D Imaging System with On-chip Depth-map Computation in 45/40nm 3D-stacked BSI SPAD CMOS," in *International Image Sensor Workshop 2021*, 2021.

[15] A. T. Erdogan, R. Walker, N. Finlayson, N. Krstajic, G. O. S. Williams, and R. K. Henderson, "A 16.5 giga events/s 1024 × 8 SPAD line sensor with per-pixel zoomable 50ps-6.4ns/bin histogramming TDC," in *2017 Symposium on VLSI Circuits*, 5-8 June 2017 2017, pp. C292-C293, doi: 10.23919/VLSIC.2017.8008513.

[16] C. Zhang, S. Lindner, I. M. Antolović, J. M. Pavia, M. Wolf, and E. Charbon, "A 30-frames/s, 252 x 144 SPAD Flash LiDAR With 1728 Dual-Clock 48.8-ps TDCs, and Pixel-Wise Integrated Histogramming," *IEEE Journal of Solid-State Circuits,* vol. 54, no. 4, pp. 1137-1151, 2019, doi: 10.1109/JSSC.2018.2883720.

[17] C. Zhang *et al.*, "A 240 x 160 3D Stacked SPAD dToF Image Sensor with Rolling Shutter and In Pixel Histogram for Mobile Devices," *IEEE Open Journal of the Solid-State Circuits Society,* pp. 1-1, 2021, doi: 10.1109/OJSSCS.2021.3118332.

[18] B. Kim *et al.*, "7.2 A 48×40 13.5mm Depth Resolution Flash LiDAR Sensor with In-Pixel Zoom Histogramming Time-to-Digital Converter," in *2021 IEEE International Solid- State Circuits Conference (ISSCC)*, 13-22 Feb. 2021 2021, vol. 64, pp. 108-110, doi: 10.1109/ISSCC42613.2021.9366022.

[19] S. Park *et al.*, "5.3 An 80×60 Flash LiDAR Sensor with In-Pixel Histogramming TDC Based on Quaternary Search and Time-Gated Δ-Intensity Phase Detection for 45m Detectable Range and Background Light Cancellation," in *2022 IEEE International Solid- State Circuits Conference (ISSCC)*, 2022.

[20] H. Seo *et al.*, "Direct TOF Scanning LiDAR Sensor With Two-Step Multievent Histogramming TDC and Embedded Interference Filter," *IEEE Journal of Solid-State Circuits,* pp. 1-1, 2021, doi: 10.1109/JSSC.2020.3048074.

[21] I. Gyongy, A. T. Erdogan, N. A. W. Dutton, and H. Mai, "A 200kFPS, 256×128 SPAD dToF sensor with peak tracking and smart readout," in *International Image Sensor Workshop 2021*, 2021.

[22] P. Padmanabhan *et al.*, "7.4 A 256×128 3D-Stacked (45nm) SPAD FLASH LiDAR with 7-Level Coincidence Detection and Progressive Gating for 100m Range and 10klux Background Light," in *2021 IEEE International Solid- State Circuits Conference (ISSCC)*, 13-22 Feb. 2021 2021, vol. 64, pp. 111-113, doi: 10.1109/ISSCC42613.2021.9366010.

[23] T. Okino *et al.*, "5.2 A 1200×900 6μm 450fps Geiger-Mode Vertical Avalanche Photodiodes CMOS Image Sensor for a 250m Time-of-Flight Ranging System Using Direct-Indirect-Mixed Frame Synthesis with Configurable-Depth-Resolution Down to 10cm," in *2020 IEEE International Solid- State Circuits Conference - (ISSCC)*, 16-20 Feb. 2020 2020, pp. 96-98, doi: 10.1109/ISSCC19947.2020.9063045.

[24] H. Ruokamo, L. W. Hallman, and J. Kostamovaara, "An 80 x 25 Pixel CMOS Single-Photon Sensor With Flexible On-Chip Time Gating of 40 Subarrays for Solid-State 3-D Range Imaging," *IEEE Journal of Solid-State Circuits,* vol. 54, no. 2, pp. 501-510, 2019, doi: 10.1109/JSSC.2018.2878816.

[25] K. Q. K. Nguyen, E. M. D. Fisher, A. J. Walton, and I. Underwood, "An experimentally verified model for estimating the distance resolution capability of direct time of flight 3D optical imaging systems," *Measurement Science and Technology,* vol. 24, no. 12, p. 125001, 2013/11/12 2013, doi: 10.1088/0957-0233/24/12/125001.

[26] A. Tontini, L. Gasparini, and M. Perenzoni, "Numerical Model of SPAD-Based Direct Time-of-Flight Flash LIDAR CMOS Image Sensors," (in eng), *Sensors (Basel),* vol. 20, no. 18, Sep 12 2020, doi: 10.3390/s20185203.

[27] L. J. Koerner, "Models of Direct Time-of-Flight Sensor Precision That Enable Optimal Design and Dynamic Configuration," *IEEE Transactions on Instrumentation and Measurement,* vol. 70, pp. 1-9, 2021, doi: 10.1109/TIM.2021.3073684.

[28] O. Kumagai *et al.*, "7.3 A 189×600 Back-Illuminated Stacked SPAD Direct Time-of-Flight Depth Sensor for Automotive LiDAR Systems," in *2021 IEEE International Solid- State Circuits Conference (ISSCC)*, 13-22 Feb. 2021 2021, vol. 64, pp. 110-112, doi: 10.1109/ISSCC42613.2021.9365961.